Pure OPM Nanofibers with High Piezoelectricity Designed for Energy Harvest In Vitro and In Vivo

Tong Li[a,#], Zhang-Qi Feng[a,b,f,#,*], Ke Yan[a], Tao Yuan[c], Wuting Wei[c], Xu Yuan[a,d], Chao Wang[e], Ting Wang[b,f,*], Wei Dong[a], and Jie Zheng[f]

[a] School of Chemical Engineering, Nanjing University of Science and Technology, 200 Xiao Ling Wei, Nanjing, 210094 , China

[b] State Key Laboratory of Bioelectronics, Southeast University, Nanjing 210096, China

[c] Department of Orthopedic, Nanjing Jinling Hospital, Nanjing, 210002, China

[d] Nanjing Daniel New Mstar Technology Ltd, Nanjing, 211200 , China

[e] Office of Science and Technology Research, Nanjing University of Science and Technology, 200 Xiao Ling Wei, Nanjing, 210094 , China

[f] Department of Chemical and Biomolecular Engineering, The University of Akron, Akron, OH 44325, USA

 * Corresponding authors. E-mail: fengzhangqi1981@163.com and

echo2165@163.com

[#] These authors contributed equally to this work.
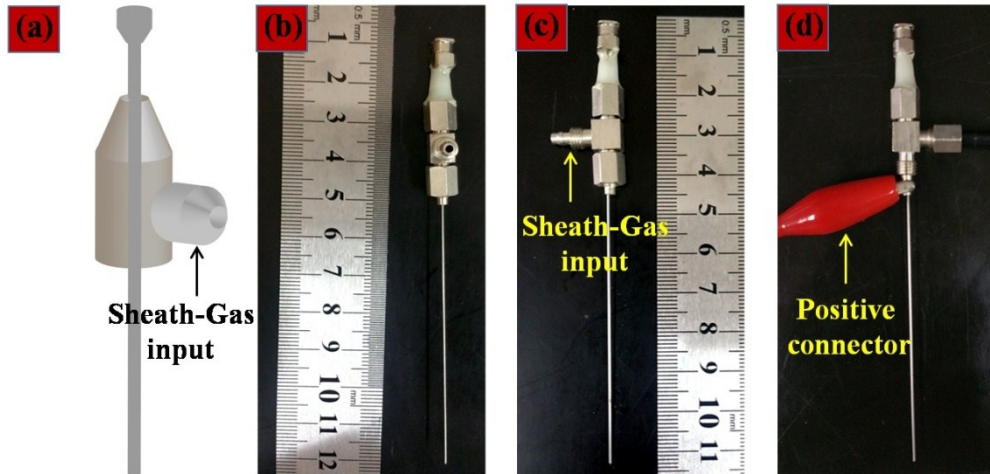
Fig. S1. (a) The perspective view of the spinneret in the sheath-gas assisted electrospinning device. (b, c) The front and side photographs of the spinneret. The injection needle passed through the air channel and sealed the end with a sealing device. (d) The photograph of the spinneret connected to the positive electrode of high-voltage power.

Assistant gas from a air channel is supplied into the spinneret through the sheath-gas input ducts to ensure the well-distributed of gas in the nozzle. The air will be guided into the nozzle and acted as sheath-gas to stretch the electrospinning charged nano-jet flow.
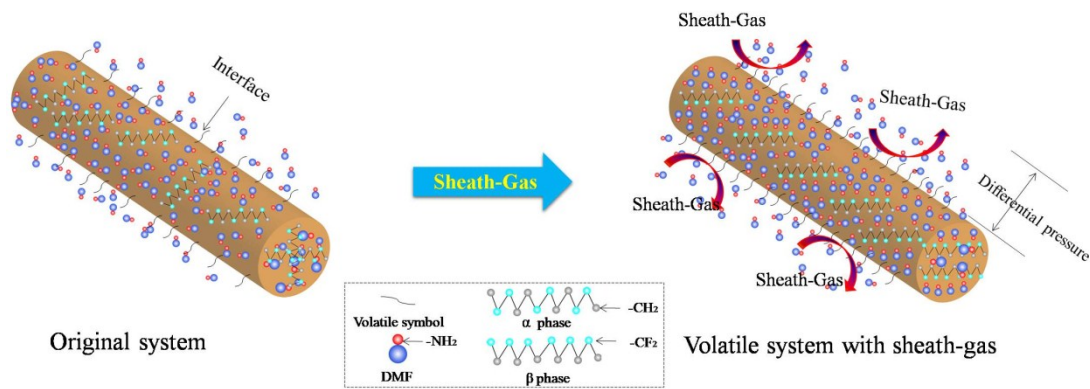
Fig. S2. Schematic diagrams of the transition from liquid solution in nanojets to solid nanofibers.

The sheath-gas can strengthen the convection and exchange between the gaseous solvents DMF, so that the solvents outside the nanofibers are continuously taken away, thereby ensuring that the evaporation surface and the outside always maintain a certain pressure difference, increasing the evaporation rate. Within a certain range, the faster the sheath-gas flow, the more favorable the convection and exchange of the solvent in the air, thereby increasing the pressure difference at the gas-solid interface. However, when the sheath-gas velocity reaches a certain level, the evaporation at the interface tends to be stable, and the effect is relatively small at this time. This theory also provides the basis for the choice of sheath-gas pressure. More importantly, due to the presence of abundant hydrogen bonds between $-NH_2$ of DMF as electrospun solvent and $-CF_2$ dipoles in the PVDF solution, the rapid evaporation of the solvent would lead to a strong tensile action in the nano-jets, which promotes the formation of a large amount of the β-phase in the PVDF/gas nanofibers that are in turn used as working dipole of piezoelectricity.
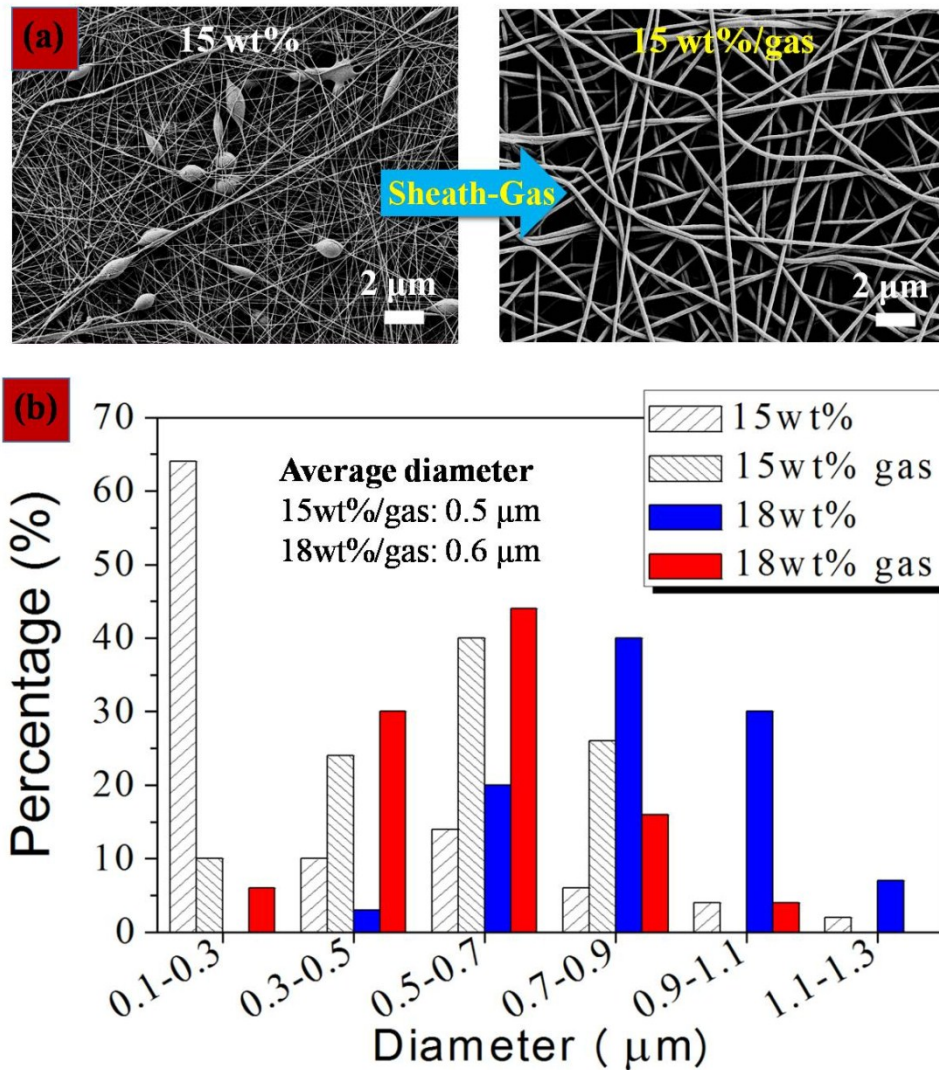
Fig. S3. (a) SEM images of the PVDF (left) and PVDF/gas (right) nanofibers and (b)their diameter distribution.

Fig. S3 showed that the sheath-gas can improve the morphology of the electrospun nanofibers. The PVDF nanofibers from the 15 wt% electrospinning solution displayed a wide variety of fiber diameters and some beads due to the lower tensile viscosity (the left of Fig. S3a). However, after treating with sheath-gas, the PVDF/gas nanofibers from the same 15 wt% electrospinning solution displayed a narrow and uniform diameter distribution (the right of Fig. S3a), with the average diameter of 0.5μm (Fig. S3b). These phenomena proved again that the sheath-gas provided an

excessive tensile force to stretch the nanofibers and a fast solvent volatilization to improve the phase transition from the α phase to β and γ phase.
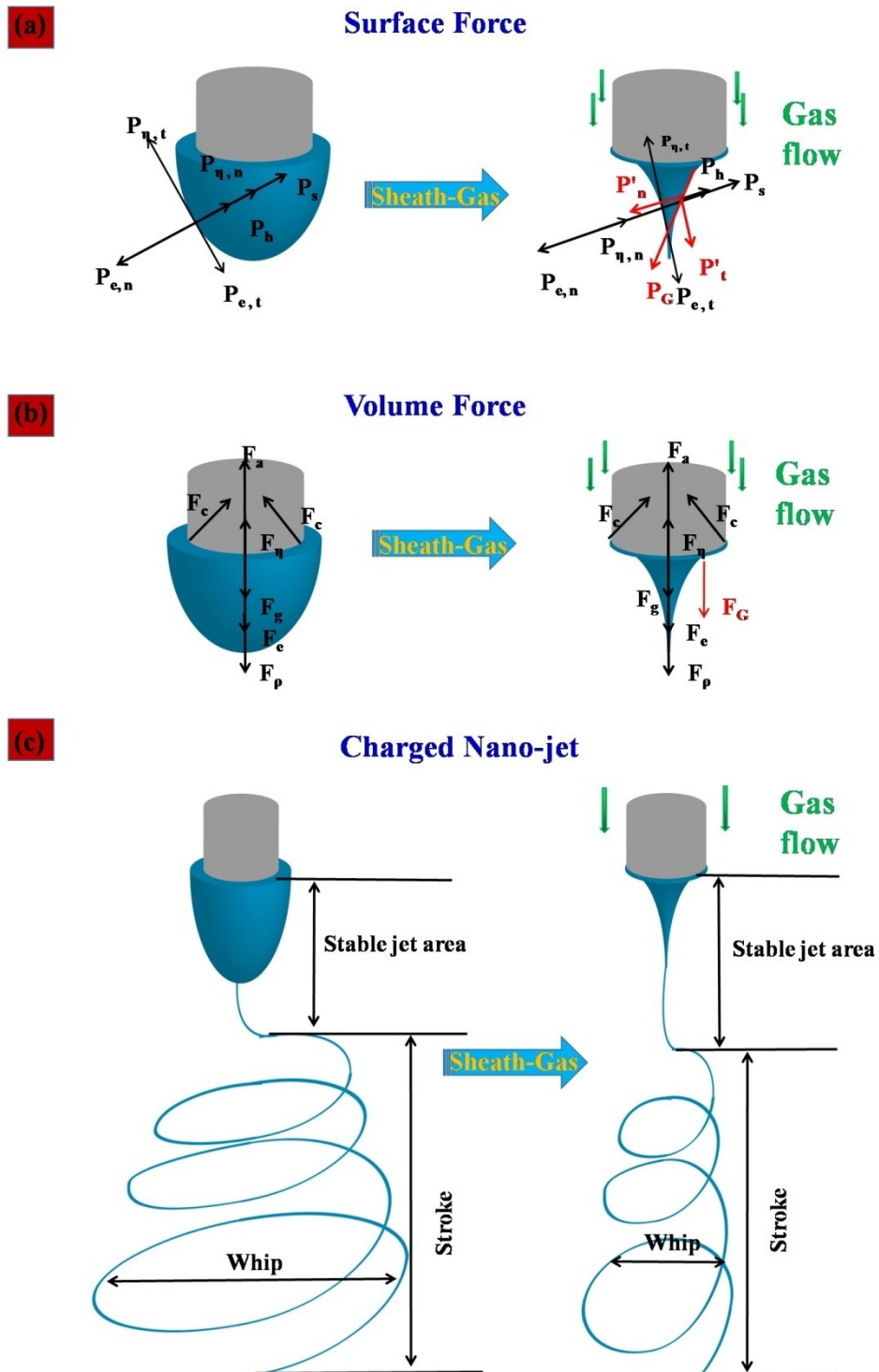
Fig. S4. (a) The surface force schematic of the Taylor cone: the conventional electrospinning process and sheath-gas electrospinning process. (b) The volume force schematic of the Taylor cone: the conventional electrospinning and sheath-gas

electrospinning process. (c) Schematic diagram of charged jet motion: the conventional electrospinning process and sheath-gas electrospinning process.

The surface normal force and tangential force of Taylor cone can be expressed by equations (1-4) as follows:

$$P_n = P_{e,n} - P_{\eta,n} - P_h - P_s \tag{1}$$

$$P_{n1} = P_{e,n} - P_{\eta,n} - P_h - P_s + P'_n \tag{2}$$

$$P_t = P_{e,t} - P_{\eta,t} \tag{3}$$

$$P_{t1} = P_{e,t} - P_{\eta,t} + P'_t \tag{4}$$

where P_n and P_t are the surface normal force and tangential force of Taylor cone caused by electric and gravitational fields, respectively. P_{n1} and P_{t1} are the surface normal force and tangential force of Taylor cone caused by sheath-gas, electric and gravitational fields, respectively. $P_{e,n}$, $P_{e,t}$, $P_{\eta,n}$ and $P_{\eta,t}$ represent normal electric field force, tangential electric field force, normal sticky stress and tangential sticky stress of Taylor cone. P'_n and p'_t are additional normal force and tangential force of Taylor conecaused by sheath-gas. P_h and P_s are static pressure of fluid and the pressure difference caused by the surface tension. Obviously, the sheath-gas provides additional force to increase both the surface normal and the tangential force (Fig. S 4a), effectively.

When the Taylor cone is spinning, the volume force of the Taylor cone could be expressed by the following equations (5,6):

$$F_v = F_g + F_e + F_\rho - F_\eta - F_a - F_c \tag{5}$$

$$F_{v1} = F_g + F_e + F_\rho - F_\eta - F_a - F_c + F_G \tag{6}$$

where F_v is the volume force of the Taylor cone generated by electric and

gravitational fields. F_{v1} is the volume force of the Taylor cone caused by sheath-gas, electric and gravitational fields. F_g, F_e, F_ρ, F_η, F_a and F_c represent gravity, electric field force, inertial force, viscous force, air resistance and capillary force, respectively. F_G is the extra volume force caused by sheath-gas. It is not difficult to find that the presence of sheath-gas increases the volume force of the Taylor cone (Fig. S 4b).

The auxiliary action of the sheath-gas can simultaneously increase the surface force and the volume force of the Taylor cone, which can increase the moving speed of the nanofibers to reduce the whipping stroke and can also limit the range of whipping (Fig. S 4c) that can enhance the rigidity of the nanofibers and further stabilize the piezoelectric phase (β/γ phase).
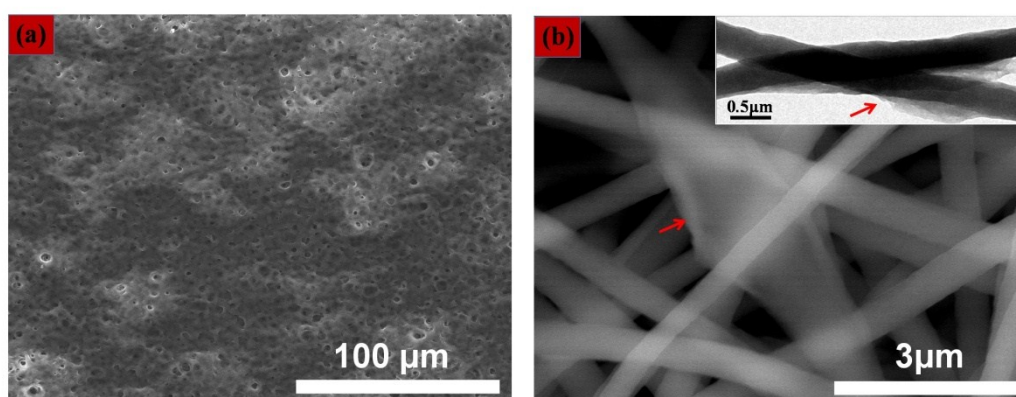
Fig. S5. (a) The SEM image showing the surface of the PVDF film. (b) The SEM image showing the rough morphology of the PVDF/GO nanofibers with 1.0 wt % GO lamellae (red arrow). The inset of (b) showing PVDF/GO nanofibers structure consisting of a PVDF core and GO shell (red arrows).
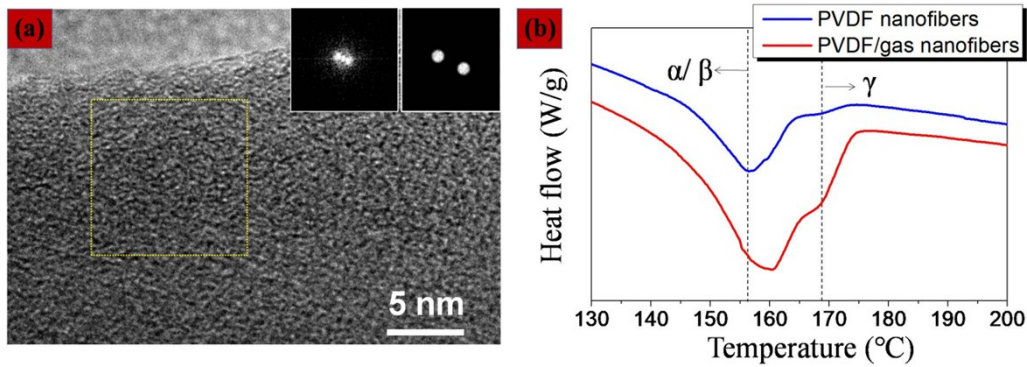
Fig. S6. (a) HRTEM image of the pure PVDF nanofiber. The inset images are the FFT before and after the mask filtering and its corresponding scanning area was shown by a yellow dotted line (the inset). (b) DSC thermograms of the pure PVDF and PVDF/gas nanofibers.

Fig. S 6b showed the DSC scans of PVDF and PVDF/gas nanofibers. The melting endotherms of α- and β-PVDF were reported to be at the similar position. Comparing to the pure PVDF nanofibers, the DSC thermograms of the PVDF/gas nanofibers present a peak melting temperature shifting toward higher temperatures and narrowing of the melting point features. The thermograms demonstrated that the sheath-gas caused an increase in the total amount of β phase in the PVDF/gas nanofibers. In addition to the spikes responding to the β phase, a small peak at 169° assigned to the γ phase appeared in the PVDF/gas nanofibers. Sheath-gas accelerated the volatilization of the solvent and achieved the rapid stretching and transformation of liquid-solid phase during the electrospinning, which could effectively transform most of the α phase into the working dipole of β phase in the recrystallization of the PVDF/gas nanofibers during the electrospinning process.
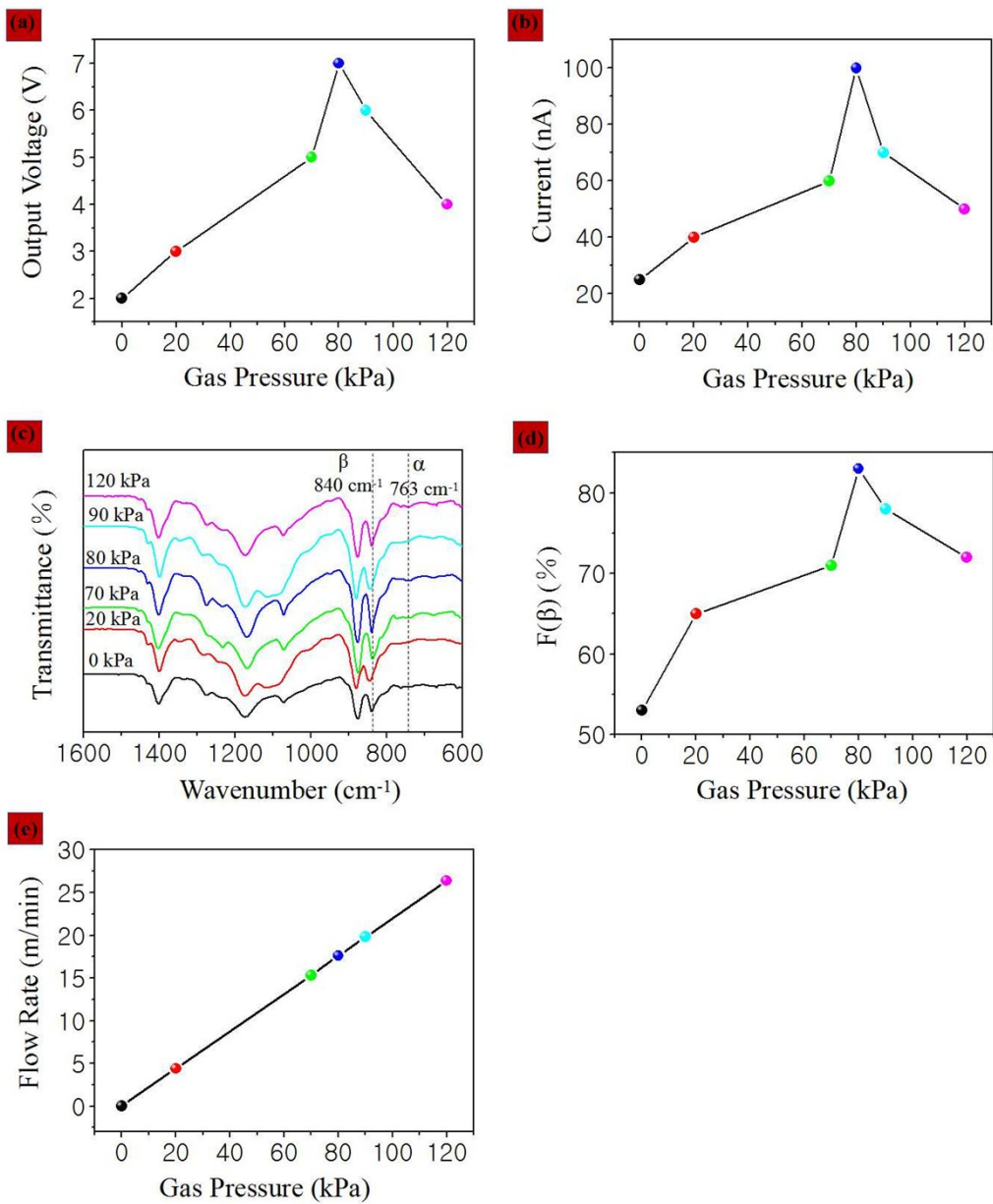
Fig. S7. (a, b) The output voltage and current signals generated by nanogenerators based on PVDF/gas nanofibers with various air pressures. (c) FTIR spectra of pure PVDF and PVDF/gas nanofibers. (d) Variation of the fraction of the polar β phase content of PVDF/gas nanofibers with various pressures. (e) The linear relationship between the gas pressure and the flow rate of the sheath-gas.

The sheath-gas is determined to be 80 kPa, because that a small pressure cannot effectively stretch the molecular chain of the PVDF, while an excessively high air pressure will provide a surplus tensile force to destroy the original molecular chain, and then decrease the piezoelectric performance of the PVDF nanofibers (Fig. S 7a and b). From the perspective of the content of the polar phases, the intrinsic cause of the change in piezoelectric performance is qualitatively resolved. The FTIR spectra show characteristic vibration bands designated for the PVDF polar phase (β phase) at 840 cm^{-1}. In contrast, the intensity at 763cm^{-1} band is assigned to quantify the relative fraction of α crystal phase. Based on FTIR result, the relative polar phase content ($F_{(\beta)}$) can be calculated using the equation (7) as follows:

$$F_{(\beta)} = A_{(\beta)}/(1.26A_{(\alpha)} + A_{(\beta)}) \tag{7}$$

where $A_{(\beta)}$ and $A_{(\alpha)}$ are the intensity of the β-phase peak at 840cm^{-1} and the intensity of the α crystal phase peak at 763cm^{-1}, respectively. The calculated polar phase content in the PVDF/gas nanofibers (80 kPa) is as high as 83%, while the content of piezoelectric phase in PVDF nanofibers is only 52%, which means that the content of piezoelectric phase is increased by about 60%. And the change trend of polar phase content is the same as that of piezoelectric output.

Ignoring the pipe roughness coefficient (i.e., the resistance), the flow rate of the sheath-gas can be calculated by equation (8):

$$V = (Q/A)*(P'/P) \tag{8}$$

where V is the flow rate, Q represents the flow rate per unit time, and A is the cross-sectional area of the sheath-gas outlet. P' is the air pressure at the inlet of the sheath-gas device, and P is the total air pressure. According to the fixed parameters of the air compressor, Q is known to be 0.11 m^3/min, and P is 800 kPa. Meanwhile,

the diameter of the sheath-gas device is known to be 0.2 mm. Finally, the sheath-gas

flow rates are calculated according to the different P', as shown in Fig. S7e.
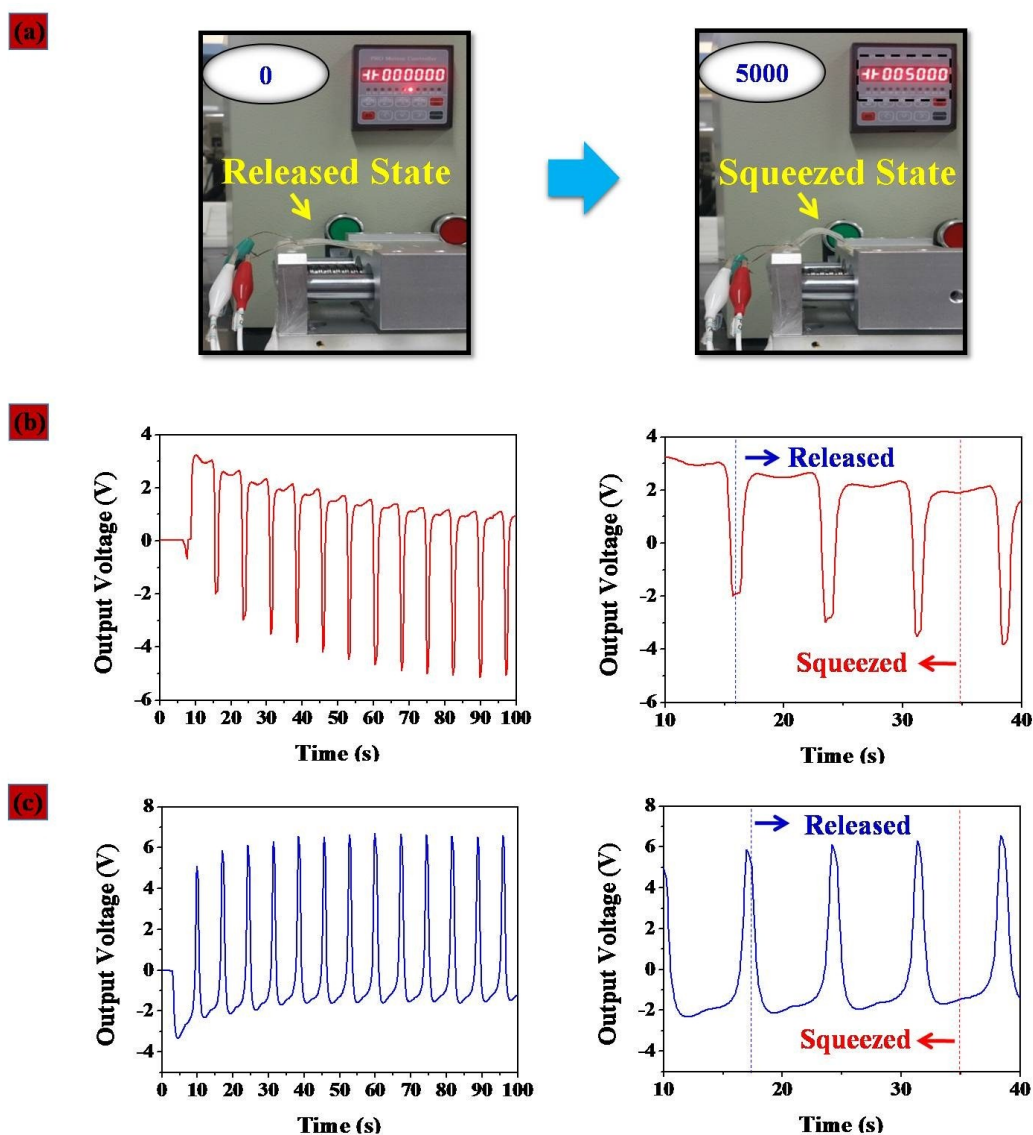
Fig. S8. (a) The experimental setup including a flexure stage controlled by a step-

motor controller to flex the sample. The extrusion displacement is 5000 pulses

(0.5cm). (b) The output voltage generated by the positive extrusion and the enlarged

view (right) of the output signal. (c) The output voltage generated by the reverse

extrusion and the enlarged view (right) of the output signal.

Once the flexible harvesting device is squeezed, piezopotential is generated inside the thin film by the tensile stress-induced deformation of the device, resulting in electrons flow in the external load to balance the electric field made by dipoles and accumulate at the top electrode. When the flexible harvesting device returns to the original flat state, the charges tend to move back to their original positions. Consequently, under periodic motions of bending and unbending, positive and negative electric signals are generated from the flexible device.
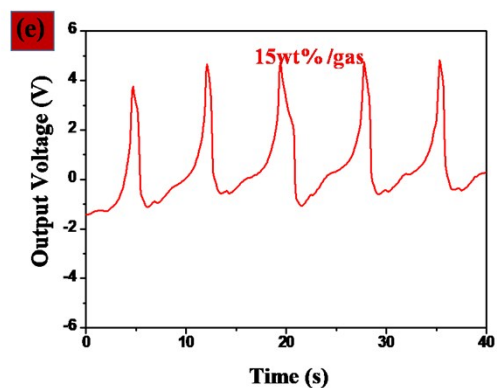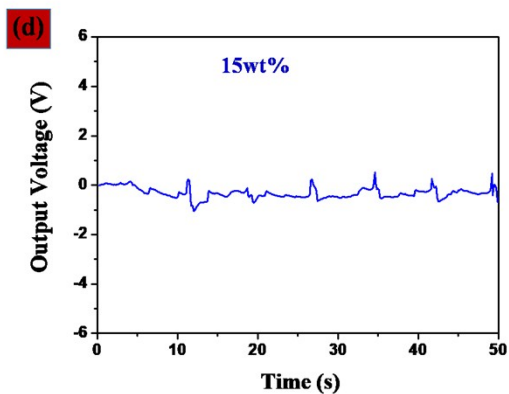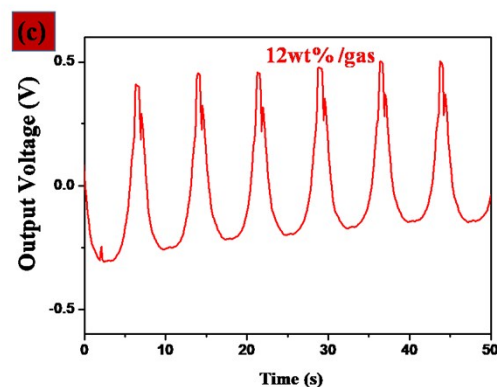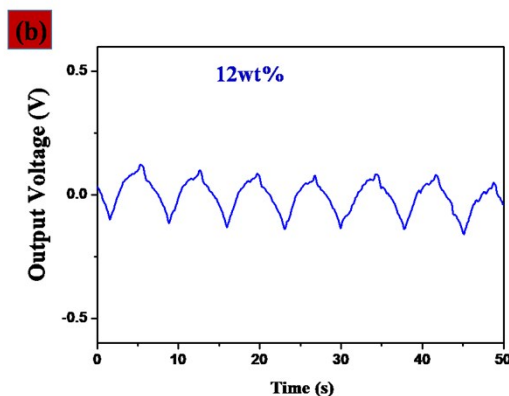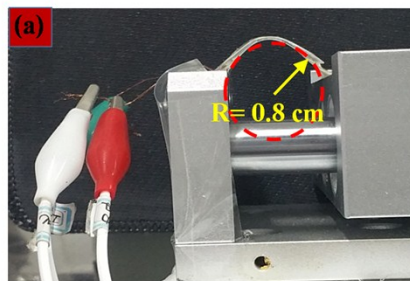
Fig. S9. (a) Schematic of the squeeze-release experiment; Output voltages of nanogenerators prepared *by* PVDF (b,d) and PVDF/gas nanofibers (c,e), respectively.

The concentration of the electrospun solution is 15 wt%. The PVDF/gas nanofibers based nanogenerator exhibited an output voltage of 5.5 V (the peak-to-peak voltage), whereas 1.5 V was observed in the sample based on PVDF nanofibers. When the concentration of PVDF was 15wt%, some beads doped in the nanofibers prevented the transfer of charge to affect the piezoelectric properties (Fig. S 3a), resulting that 87.5% duty ratio was achieved which indicated a low mechanical-electric conversion rate. Under the purging of the sheath-gas, not only can provide the internal/external stress to improve the ratio of piezoelectric phases, but also can reduce the existence of droplets. In short, the output voltage was significantly increased through the purge of sheath-gas, almost 3.5 times. Similarly, the same conclusion was reached for 12 wt% PVDF solution.
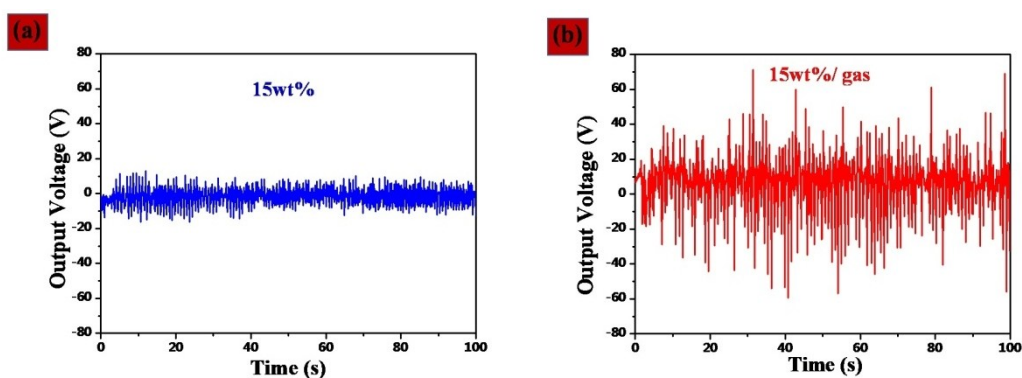
Fig. S10. (a,b) The short circuit currents of the nanogenerators prepared with PVDF and PVDF/gas nanofibers, respectively, corresponding to the maximum bending state of the finger.

The concentration of the electrospun solution was 15 wt%. The currents generated from the nanogenerators based on PVDF and PVDF/gas nanofibers were about 20 nA and 70 nA (the peak-to-peak current) under the corresponding the maximum bending of finger (~120°), respectively.
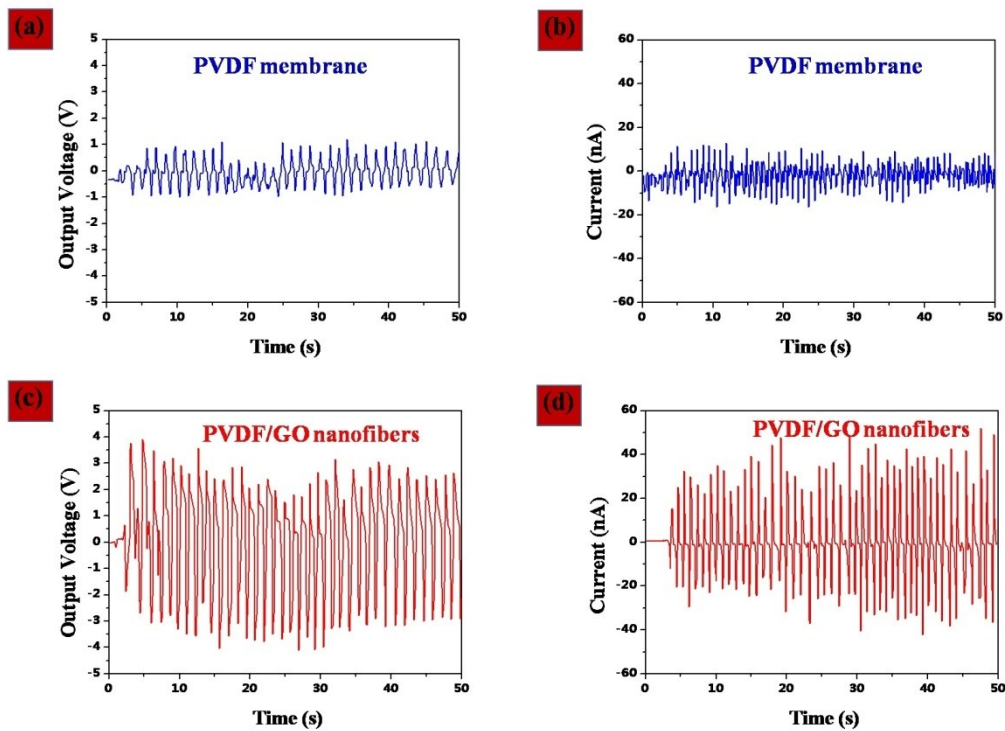
Fig. S11. (a) The output voltage and (b) the current of nanogenerators based on PVDF membrane. (c) The output voltage and (d) the current of nanogenerators based on PVDF/GO nanofibers. The above operating power was 0.8HZ.
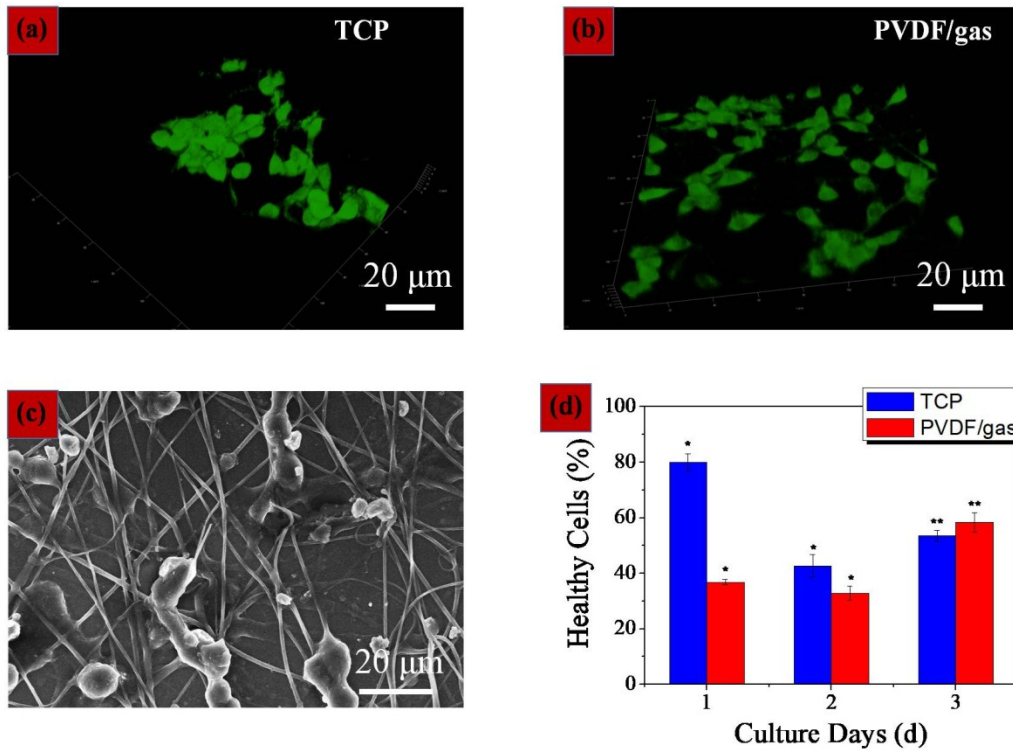
Fig. S12. Three-dimensional confocal scans of cells on   the tissue culture plate (a) and PVDF/gas nanofiber scaffolds (b), respectively. (c) SEM image of morphology of the cultured PC 12 cells on the PVDF/gas nanofibers. (d) MTT assay showing no indications of toxicity for cells on PVDF/gas nanofibers at day 3. (*P value ≤0.05, **P value ≤0.01) Error bar is calculated standard error.

The PVDF/gas nanofibers were directly electrospun on round glass sheets with similar pore size to the culture plates. We divided the experiments into two groups, namely the tissue culture plate (TCP) and PVDF/gas nanofibers. The glass sheets with nanofibers were soaked in 75% alcohol for 30 minutes, and then transferred to the corresponding culture plates, which was sterilized by ultraviolet light irradiation for 1h. The above operations were performed in a sterile operating table.

PC 12 cells were cultured in the environment of 37 ℃ and 5% CO_2 in DMEM with 10% FBS, 1% penicillin, 1% glutamine, and 0.01% fungizone until confluence. PC 12

cells were then seeded at a density of 5 x 10^4 cells/ml in a culture plate. We set TCP as a control group, while the PVDF/gas nanofibers was the experimental group. Three parallel experiments were set up in the experimental group and the control group, and 500 μL cells suspension was added to each well. The plates were incubated in a 5% CO_2 incubator at 37 ℃ for 3 h to allow the cells to adhere, and then 500 μL fresh medium was added to each well for further incubation. The activity of the cultured PC 12 cells was analyzed using a 3-(4, 5-dimethylthiazol-2yl)-2, 5-diphenyl-2H-tetrazolium bromide (MTT) assay. The cells were first incubated with MTT solution (100 μL) in an incubator at 37 °C for 3 h. Then, the culture medium was removed, and the insoluble formazan was dissolved in 500μL dimethyl sulfoxide (DMSO) solvent in each well. The absorbance of the solution was measured using a microplate reader (Multiskan MK3, Thermo Fisher Scientific Inc., USA) at a wavelength of 490 nm. The cell membrane was stained with dye DiO. Specifically, the PC12 cells were fixed for 15 min in the cell incubator after cell staining, then washed three times with warm Phosphate Buffered Saline (PBS), and the associated fluorescent photographs were taken by inverted laser scanning confocal microscopy (LSCM, SP8, Leica).

From the three-dimensional fluorescence plot, it was found that PC12 cells agglomerated in TCP (Figure S12a), while in the PVDF/gas nanofiber system, PC12 cells were uniformly dispersed in the culture plate (Figure S12b), which was further verified by the SEM image. As shown in Fig. S12c, the cell aggregates are tightly bound to PVDF/gas nanofibers under the observation of SEM images. More importantly, even if the cells still had good cell activity after three days (Fig. S12d), it could be initially verified that the PVDF/gas nanofibers could be safely used in vivo.